
Collaborative Blind Image Deblurring

Thomas Eboli Jean-Michel Morel Gabriele Facciolo

Université Paris-Saclay, ENS Paris-Saclay, CNRS, Centre Borelli, France

https://github.com/teboli/collaborative_blind_deblurring

Abstract

Blurry images usually exhibit similar blur at various locations across the image domain, a property barely captured in nowadays blind deblurring neural networks. We show that when extracting patches of similar underlying blur is possible, jointly processing the stack of patches yields superior accuracy than handling them separately. Our collaborative scheme is implemented in a neural architecture with a pooling layer on the stack dimension. We present three practical patch extraction strategies for image sharpening, camera shake removal and optical aberration correction, and validate the proposed approach on both synthetic and real-world benchmarks. For each blur instance, the proposed collaborative strategy yields significant quantitative and qualitative improvements.

1 Introduction

Image deblurring is the problem of predicting sharp images from blurry ones. In the most common case, a single blurry image is available, and the goal is to predict its sharp version. Except in rare situations where the blur is known, *e.g.*, via embedded hardware [36] for camera shake, or via lens calibration [5] for lens blur, we have little information on the blur. This blind setting is highly ill-posed and requires priors over both the latent sharp image and the blur to be solved [29]. Classical approaches to blind deblurring leverage image and blur kernel priors to first estimate the blur kernel, and second estimate a sharp image via non-blind deblurring. The best priors for doing so, *e.g.*, [34], are based on picking the salient edges across the image that provide high-quality hints on the blur [22].

Yet, ever since the introduction of large corpora of sharp/blurry image pairs such as the GoPro dataset [33], neural networks achieve state-of-the-art deblurring results. They are trained to predict a sharp image directly from a blurry input, without requiring the intermediate estimation of the blur kernel. To do so, the network may need to extract some relevant features of the blur in order to predict correctly the missing high frequencies. The hints needed to determine the blur (the edges [22]) are usually spread across larger regions of the image than what is captured by the receptive fields of convolutional networks. This is a reason why the multi-scale architectures [10, 33] are so widespread for this task. Self-attention [41] can collect such widespread hints, however they are too expensive to deploy in realistic scenarios with large images [30]. Despite impressive results, none of these approaches truly leverage the existing image processing expertise. These sparse hints are well exploited by classic methods either by exploiting the global property of the Fourier transform [20] or by analyzing the directional gradient histogram of the image [14].

In this work we propose to feed the network the relevant hints needed to improve the ability of the model to extract the blur from the representation of the blurry image. We propose a collaborative scheme where the network jointly processes several patches with the same underlying blur as a way to disambiguate the blur. Increasing the number of patches increases the probability of collecting all the useful information needed to deblur. Collaboration happens by a sort of “attention-without-attention” module, which amounts to selecting relevant patches for the task at hand. For instance, in the case of

motion deblurring, patches coming from the same moving object. Note that the patches can come from locations thousands of pixels apart, which is in practice hardly achievable by convolutions or attention. We show that collecting such sets of patches sharing similar underlying blur is straightforward for three practical instances of blur: camera shake [44], optical aberrations [39] and mild blurs [14]. Within the network, this collaboration is achieved by processing the patches in parallel and by inserting pooling layers that foster the collaboration between the encoded features. Our experiments show that this collaborative processing boosts the deblurring accuracy of the network. This strategy can be applied to a variety of architectures. A practical application of our technique illustrated in this paper is designing lightweight yet efficient blind deblurring networks.

Our contributions are summarized as follows: (1) We propose a collaborative strategy that consists in gathering a stack of patches with similar underlying blur in an image, and jointly processing them in a neural network upgraded with a layer pooling along the stack dimension. (2) We show its practicality for three instances of blur: camera shake, optical aberrations and mild blurs. (3) We provide theoretical elements to connect the proposed approach to existing classical blind deblurring methods. (4) We show on both real-world and synthetic data the efficiency of the approach for the three sorts of blur listed above, and validate two elements of design: how many patches should collaborate and which pooling function to use.

2 Related work

Classic blind image deblurring algorithms alternate between a kernel-estimation step, and a non-blind deblurring step [29]. At each step the estimated kernel is used to recover a sharper image by the non-blind deblurring, which in turn is used to refine the kernel prediction. The kernel prediction makes use of domain knowledge such as smoothness and sparsity of camera shake [44], approximate symmetry of optical aberration [39], the Gaussian shape of defocus blur [21] or translational motions in street photography [12]. The work of Nah *et al.* [33] adopts instead a black-box paradigm by learning from a large dataset of aligned blurry and sharp image pairs a multi-scale CNN that predicts from a single blurry image a restored variant, without the need for traditional image priors or any explicit structure on the family of blur to remove. The properties on the blur are now determined by the training dataset, for instance camera shake [38], defocus [1] or dynamic motions [33]. Subsequent architectures follow this trend by introducing recurrent layers [40], additional skip connections [19, 35], attention modules [10, 42], adversarial losses [24], patch-aware normalization layers [11], and more recently diffusion models [15, 43]. Similar deep learning-based strategies have been since proposed for defocus [1] and optical aberration [9] correction consisting in both collecting large real-world supervisory datasets and designing ad-hoc models. In this work, we combine knowledge of a certain kind of blur, *e.g.*, camera shake, out-of-focus blur, optical aberration, and blind deblurring networks by grouping patches from an input blurry image. We explicitly make them interact within an architecture whose design is inspired by the burst deblurring approach of [3], yet for restoring a *single* image.

Using multiple images or patches from a single image to disambiguate restoration is common in image processing. Image collaboration is crucial for system-specific degradation such as vignetting correction [27], camera calibration [46] or fixed pattern noise estimation [8]. Nevertheless the most notable example of collaborative image processing is the BM3D [13] denoising algorithm that gathers patches with similar aspect to denoise them together. In the same spirit burst deblurring methods [3, 16] combine multiple frames depicting the same underlying sharp image but different blurs. Our approach is a single-image method that can be seen as the *dual* problem of burst deblurring: we select patches of different underlying sharp contents but sharing identical or similar blurs. This aims at obtaining information on the blur in as many directions as possible thanks to a greater variety of directional gradients from the different images/patches to better predict a blur kernel, a general idea considered in previous works [14, 17, 20, 32]. To our knowledge this philosophy is explicitly applied to single-image blind deblurring via neural networks for the first time in this paper.

3 Theoretical background

To motivate our approach we review the problem of kernel estimation from several samples. Let x_1, x_2, \dots, x_N be N sharp images, y_1, y_2, \dots, y_N corresponding blurry images where $y_n = k * x_n + \varepsilon_n$ for n in $\{1, \dots, N\}$, k a blur kernel, and the ε_n 's instances of noise. From the pairs (x_n, y_n)

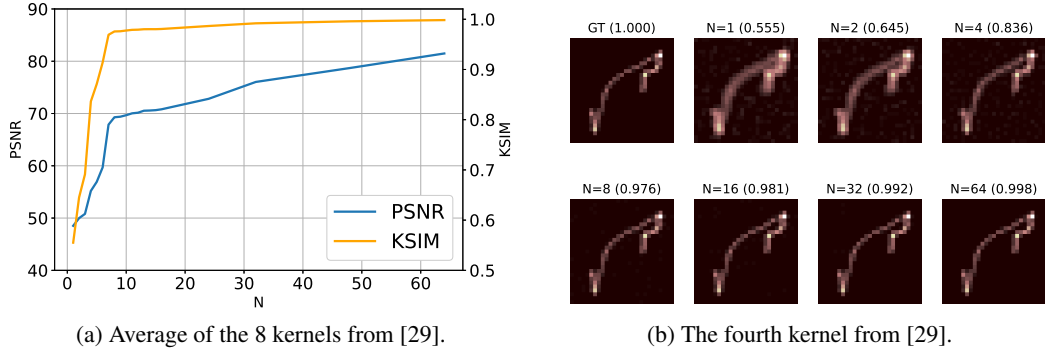


Figure 1: Illustration of the collaborative scheme with the kernels from [29]. We report the PSNR and the kernel similarity (KSIM) as defined in [45] on the left and the KSIM for each qualitative kernel on the right. Combining more sharp/blur pairs dramatically improves the accuracy of the kernel support, with saturation occurring at $N = 8$.

($n = 1, \dots, N$), we estimate the blur kernel k by minimizing a regularized ℓ_2 energy function:

$$\min_k \frac{1}{N} \sum_{n=1}^N \|y_n - k * x_n\|_2^2 + \lambda \|k\|_2^2. \quad (1)$$

Its unique minimizer may be obtained in the Fourier domain by

$$\hat{K} = \sum_{n=1}^N X_n^* Y_n / \left(\sum_{n=1}^N X_n^* X_n + \lambda N \right), \quad (2)$$

where the capital letters X_n , Y_n and K denote the Fourier transforms of x_n , y_n and k , the $*$ superscript denotes the complex conjugate, and λ is a positive regularization weight. In the Fourier domain, the multiplication and division are entrywise. In this setting, even if one image X_n has a zero at a given frequency, the average of several images would likely not be zero, unless the frequency is removed by the blur kernel. When $N = 1$ instead, if there is ambiguity at some frequencies (the blur may be oriented in the same direction as an edge for instance), then it is nearly impossible to recover the correct frequency of the blur kernel. On the spatial domain, considering more images thus boils down to gathering as much information on the oriented gradients as possible to disambiguate the blur from the signal, a strategy at the core of certain blind deblurring techniques [14, 20].

Let us illustrate how important it is to use N image pairs *together* using Eq. (2). We select the 512×512 central crops of the 64 first RGB test images from the DIV2K dataset [2] as sharp images x_n ($n = 1, \dots, 64$) in order to have all the images at the same format. We blur them with the 8 kernels from the Levin dataset [29], and add 1% white Gaussian noise. Figure 1 illustrates the increase of the accuracy of the kernel support with respect to N for the 8 kernels from [29]. The results confirm that as the number of images in the stack increases, the performance improves significantly, leading to a nearly perfect reconstruction of even challenging a motion blur kernel. Notably, the performance saturates at a relatively small stack size of $N = 8$. This analysis highlights the dramatic improvement that collaboration among images with the same blur can bring towards better deblurring.

4 Proposed method

In this section we address the more realistic blind deblurring case, where only the blurry images y_1, \dots, y_N are available. We thus cannot rely directly on Eq (2) to improve the kernel estimation. We instead leverage the collaboration of N blurry images, as highlighted in the previous section, in order to better capture the structure of the blur while at the same time deblurring. This collaborative processing results in an efficient single-image blind deblurring neural network.

4.1 Collaborative architecture

We propose a neural network f_θ with parameter θ that features two notable changes compared to typical single-image blind deblurring networks, *e.g.*, [33]: (i) N inputs and outputs instead of a single

one, and (ii) an inner collaboration layer combining the N feature maps. When N is 1, the proposed framework boils down to the classical single-image blind deblurring approach.

Input and output. We propose a neural network that processes in a single forward pass N images $\mathcal{Y}_N = \{y_1, \dots, y_N\}$ containing similar blurs (not necessarily the exact same for each image), and predicts N sharp versions $\hat{\mathcal{X}}_N = \{\hat{x}_1, \dots, \hat{x}_N\}$. In practice these sets are implemented as 4D tensors concatenating all the RGB images of the stacks, the first dimension being of size N . Let f be such a network and θ its parameter, then the inference reads

$$\hat{\mathcal{X}}_N = f_\theta(\mathcal{Y}_N). \quad (3)$$

During training, the N restored patches have collaborated and can thus be supervised individually since what matters in the end is the quality of each individual image \hat{x}_n ($n = 1, \dots, N$). Provided training pairs of sets $\mathcal{X}_N^{(m)}$ and $\mathcal{Y}_N^{(m)}$ ($m = 1, \dots, M$), we learn the parameter θ by minimizing:

$$\min_{\theta} \frac{1}{MN} \sum_{m=1}^M \sum_{n=1}^N \ell(\hat{x}_n^{(m)}, y_n^{(m)}), \quad (4)$$

where ℓ is a pixelwise loss. In this work, we adopt the ℓ_1 distance as supervising loss function. The images $\hat{x}_n^{(m)}$ and $y_n^{(m)}$ are the n -th elements of respectively $\hat{\mathcal{X}}_N^{(m)}$ and $\mathcal{Y}_N^{(m)}$.

Inner collaboration. We follow the approach of Aittala and Durand [3]. This approach applies the same convolution layers to each one of the N images of the stack and combine the knowledge from different images in the same stack via pooling of the individual blurry images’ representations after a given convolutional or attention layer in a network. Let e_n be the representation of the n -th blurry image y_n ($n = 1, \dots, N$) after this given layer of f_θ . We implement the inner collaboration layer by a pooling function p operating on the e_n along the stack dimension, and that returns a global representation g of the stack:

$$g = p(\{e_1, \dots, e_N\}). \quad (5)$$

The feature g has the same dimension as an individual local feature e_n ($n = 1, \dots, N$). In [3], in the context of burst deblurring, g is supposed to extract a representation of the underlying sharp signal since all the blurry frames in the burst have different blurs but share the same underlying sharp content. In our case the roles of the images and blurs are reversed: we have images of different contents sharing similar blurs in our stack. Consequently, we expect the global information compiled in g via the pooling function p to be related to the blur. Lastly, the local features e_n ($n = 1, \dots, N$) are updated through the merge with the global representation g via a 1×1 convolution layer:

$$e_n \leftarrow \text{conv}_{1 \times 1}(\{e_n, g\}), \quad \forall n \in \{1, \dots, N\}. \quad (6)$$

That way, we expect the upgraded feature map e_n to be guided by some information on the blur, ultimately improving the deblurring ability of f_θ .

The function p has not been explicitly defined so far on purpose. Such a function should take a stack of spatial feature maps and return a single spatial feature map. Since no assumption is made on p , it can be either learning-free or learnable. Classical pooling strategies such as the mean or max functions are used in [3] and are drop-in candidates to extract g in our context. We also explore in this paper how to learn p by implementing it with the lambda layer from [6] or the self-attention (SA) module [41]. The learning-free approach is important to build small models that may be deployed on devices like smartphones [31], whereas the learnable modules aim at better performance at the cost of additional computations. We benchmark the different candidates for p in Section 5.

4.2 Gathering images with similar underlying blurs

The theoretical background of the previous section and its proposed integration within a neural network assume that N images y_n ($n = 1, \dots, N$) degraded with similar blurs are given. For camera shake [44], mild blurs [14] (covering out-of-focus and sharpening), and optical aberrations [18], such patches may be handpicked from a *single* image. For camera shake the blur smoothly varies across the field of view [44], and for “reasonable” shake like small translations featured in the Realblur dataset [38], it boils down to a uniform blur kernel applied to the whole image: any crop in the image therefore has the same blur. Rough uniformity of the blur is also a typical assumption for modeling

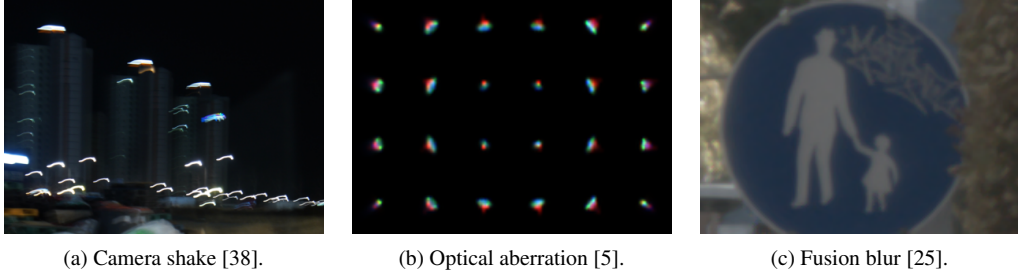


Figure 2: Three real instances of blur: camera shake from the RealBlur dataset [38] (scene 118, image 2), a subset of the local calibrated optical aberrations from the Canon EF24mm f/1.4L USM opened at f/2.8, calibrated in [5], and the result of the $\times 2$ multi-frame super-resolution online demo of [25]. For shake the light streaks suggest the blur is roughly the same everywhere, thus patches can be sampled uniformly. The same holds for fusion blur where the fused image globally lacks of sharpness. The aberrations are all unique but roughly follow a central symmetry, thus easy to sample.

lack of sharpness in the image, *e.g.*, because of a failing autofocus or the interpolation blur of a preceding multi-frame algorithm [28].

For instance, inevitable blur may come from optical aberrations [17, 23]. Very similar blurs may be found at symmetric locations on the field of view [39]. Sharpening is another instance of important brick in most ISP pipelines nowadays [14], and consists in removing small Gaussian-like blurs caused by slight out-of-focus or multi-frame fusion algorithms. The blur may vary but it may be considered roughly similar across the field of view, for instance to remove the fusion blur introduced by multi-frame algorithms [17]. A third common category is camera shake [44] during exposure, resulting in global motion blur across the image. A single blur kernel [38] or smoothly varying blurs [44] may model the whole shake, thus validating the assumption of similar kernels across the image. An illustration is shown in Figure 2. In the three common sorts of blur list above, grouping patches with similar blur is thus feasible by leveraging the properties of the blur. Collecting patches that way amounts to finding the most relevant patches for a given deblurring task, which is a sort of handcrafted attention or “attention-without-attention”. Grouping in that manner patches, which may be hundreds or thousands of pixels away from each other, is indeed doable with CNNs or attention, but at the cost of either very deep models or important computation, all that for computing something that could be known in advance.

Note that we have not discussed defocus blur where local kernels of similar aspect might be easily grouped if the depth of the scene is known [21], for instance with recent monocular depth estimators, *e.g.*, [37]. Nevertheless, we keep this multimodal approach for future work and focus instead on sorts of blurs where the grouping can be done manually as for the examples in Figure 2.

5 Experiments

Experiments were all run on a single 16Gb NVIDIA V100 graphic card. Descriptions of the training and evaluation protocols, and qualitative results are in the supplementary material.

5.1 Collaborative model

In this work, we use a UNet model that is a general architecture used as the foundation of many practical deblurring models, *e.g.*, [9, 26]. Since it is an all-purpose model, it has no specific bias for removing blur in contrast to the state-of-the-art CNNs [10, 40]. It is thus an adequate model to measure the impact of the proposed collaborative scheme. We introduce two variants called UNet and UNet-T (for tiny) embedding respectively 4 and 3 downsampling/upsampling layers in the encoder/decoder: The initial number of feature maps C is 64 and the respective bottleneck sizes of these models are 512 and 256 channels. These models have respectively around 17M and 4.3M parameters. Before each down/upsampling module we place p to enforce collaboration.

So far we have only presented the broad idea that features should be shared within p , but we did not delve into details. We compare the max pooling approach of [3] for burst deblurring, the lambda

layer [6] and a self-attention (SA) layer as in the Transformer architecture [41]. The lambda layer is implemented with 4 feature channels. The three-layer perceptron of the SA layer is shaped as an inverted bottleneck. We also evaluated the feature mean to implement p but observed as in [3] that it leads to the same results as the max pooling. Diagrams are in the supplementary material.

5.2 Validation on Gaussian blur

We start with 2D anisotropic Gaussian blur kernels that may approximate several instances of real-world blur such as lens blur [23], defocus [21], and translational motion blur [14]. Evaluating our approach on Gaussian blur is thus a simple manner to validate our approach in a controlled setting that corresponds to many real-world blurring scenarios. We train UNet and UNet-T on 128×128 crops randomly sampled from the 800 training images of the DIV2K dataset [2]. We randomly flip and rotate the patches prior to blurring them with Gaussian blur kernels of standard deviation along the two principal axes uniformly sampled in $[0.3, 4]^2$, *i.e.*, up to a 33×33 blur spot, and the orientation is uniformly sampled in $[0, 2\pi)$ (same model as in [14]). We add moderate Gaussian noise with standard deviation randomly sampled in $[0.5, 2]/255$ after blurring.

N	UNet	UNet-T
1	32.75	32.46 (-0.29)
2	32.91	32.75 (-0.16)
4	32.92	32.92 (+0.00)
8	33.12	33.13 (+0.01)
16	33.02	33.07 (+0.05)

Table 1: Average PSNR over 400 images blurred with isotropic Gaussian blur. UNet-T achieves the same performance as UNet for $N \geq 4$ despite having 4 times more parameters.

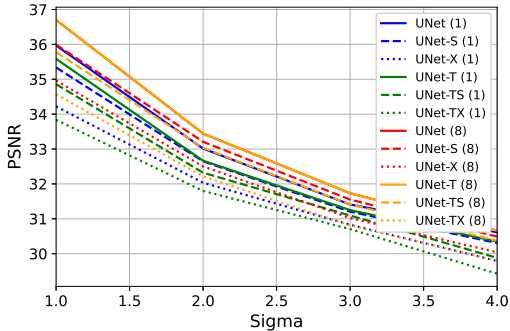


Figure 3: PSNR of UNet and UNet-T for 3 widths. N is in parenthesis. For each width, the models with $N = 8$ are above. The plain red curve is covered by the orange one.

Image stack size N . In order to evaluate the choice of the stack size N , we train networks with input stacks of blurry images sharing the same blur with a unique stack size N in $\{1, 2, 4, 8, 16\}$. We choose the max pooling strategy to not introduce additional learnable parameters, and isolate the impact of using several patches together. We train the models for 250k iterations with the Adam optimizer and initial learning rate of 5×10^{-5} that is reduced by 0.5 after each 40k iteration until reaching 10^{-6} where we observe convergence. We evaluate the models on sets of 100 images blurred with an anisotropic Gaussian blur kernel with standard deviation σ in $\{1, 2, 3, 4\}$, and with additional $0.5/255$ Gaussian noise. We show in Table 1 that the performance of both models grows with N . For $N \geq 4$, the performance of both models is similar despite UNet having 4 times more parameters than UNet-T. All the results are averaged over 3 shuffles of the test images to draw different images per N -sized stack across different runs, but the error bars are marginal and thus not reported.

Reducing UNet. Since using N images instead of 1 actually compensates the difference of depth and parameters between UNet and UNet-T for $N \geq 4$, we also verify that by reducing the width of the UNet, using $N = 8$ images helps to maintain good performance. Besides training UNet (resp. UNet-T) with the original number of channels per feature like in the previous experiment, we propose the Slim and Extra-Slim variants dubbed UNet-S and UNet-X (resp. UNet-TS and UNet-TX) where the number of channels for each feature map is respectively divided by 2 and 4, *i.e.*, the bottleneck layer of UNet initially having 512 channels has now respectively 256 and 128 channels. For $N = 1$, these models have respectively 4.4M, 1.1M, 1.1M and 270K parameters, and about 5% more for $N > 1$ (because of the 1×1 convolution layers in Eq. (6)). We train the four new variants of UNet and UNet-T with the same procedure, evaluate them on the same 400 test images as previously, and show the average PSNR per value of σ in Figure 3. It can be seen that the models with $N = 8$ systematically achieve better results than their $N = 1$ counterparts. Remark that UNet-TX for $N = 8$ achieves results similar to models that have $\times 4$ more parameters, and is between +0.3 and +0.8dB

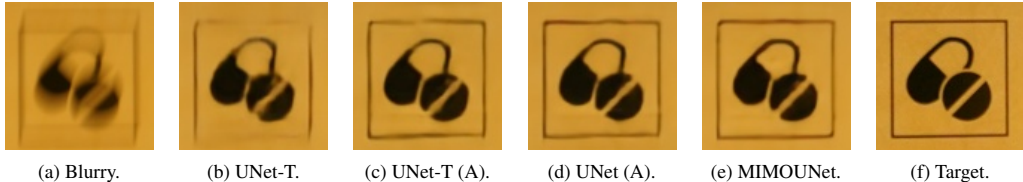


Figure 4: An example from Realblur-J [38] deblurred with UNet-T, the versions of UNet and UNet-T embedding attention with $N = 16$ and MIMOUNet [10]. The collaboration improves the deblurring accuracy of UNet, to match that of MIMOUNet.

Method	PSNR	SSIM	LPIPS	Params
DeblurGAN-v2* [24]	29.69	0.870	-	-
SRN* [40]	31.38	0.909	-	6.8M
MIMOUNet [10]	30.32	0.897	0.097	6.8M
UNet-T ($N = 1$)	29.30	0.870	0.133	4.3M
UNet-T ($N = 4, M$)	29.88 (+0.58)	0.883 (+0.013)	0.121 (-0.012)	4.6M
UNet-T ($N = 16, M$)	30.33 (+1.03)	0.893 (+0.023)	0.108 (-0.025)	4.6M
UNet-T ($N = 4, L$)	29.96 (+0.66)	0.885 (+0.015)	0.117 (-0.016)	5.6M
UNet-T ($N = 16, L$)	<u>30.45</u> (+1.15)	<u>0.896</u> (+0.026)	<u>0.104</u> (-0.029)	5.6M
UNet-T ($N = 4, A$)	30.13 (+0.83)	0.888 (+0.028)	0.111 (-0.022)	6.4M
UNet-T ($N = 16, A$)	30.63 (+1.33)	0.900 (+0.030)	0.098 (-0.035)	6.4M
UNet ($N = 1$)	30.16	0.893	0.104	17.7M
UNet ($N = 4, M$)	30.45 (+0.29)	0.897 (+0.004)	0.104 (-0.000)	18.7M
UNet ($N = 16, M$)	30.62 (+0.46)	0.900 (+0.007)	0.099 (-0.005)	18.7M
UNet ($N = 4, L$)	30.61 (+0.45)	0.900 (+0.007)	0.098 (-0.006)	22.9M
UNet ($N = 16, L$)	<u>30.78</u> (+0.62)	<u>0.904</u> (+0.011)	<u>0.094</u> (-0.010)	22.9M
UNet ($N = 4, A$)	30.73 (+0.57)	0.904 (+0.011)	0.092 (-0.012)	26.4M
UNet ($N = 16, A$)	30.98 (+0.82)	0.908 (+0.015)	0.087 (-0.017)	26.4M

Table 2: Results on Realblur-J [38]. The models with * are those reported in [38] and are used as setters of the expected ballpark of metrics. MIMOUNet [10] is retrained following our protocol. Bold and underlined numbers indicate which variants of UNet are the best and second-to-best per UNet model. The difference with the corresponding UNet(-T) with $N = 1$ is shown in parenthesis.

above its $N = 1$ counterpart. This observation suggests that the learning-free max pooling operation helps to design lightweight blind deblurring networks with performance on par with larger ones. UNet-TX has a number of parameters comparable to that of the lightweight demosaicking networks proposed in [31], which is akin to edge computing. This suggests that UNet-TX may be a valid candidate to replace mild blur deblurring algorithms, *e.g.*, [14, 17], in terms of parameters and thus energy consumption. More quantitative results are in the supplementary material.

5.3 Practical applications

We illustrate the method on the three practical problems listed in Figure 2: optical aberration correction, camera shake compensation, and image sharpening.

Camera shake. An important source of blur in personal photography (especially with handheld smartphones) is camera shake. We train on the RealBlur-J dataset [38], composed 3760 sharp/blurry image pairs of static scenes taken with complex natural camera motions, a UNet with and without the collaborative layer, and the MIMOUNet [10] specifically designed for this task. Our goal here is not to propose new state-of-the-art motion blur models, but rather use the RealBlur dataset as a real-world quantitative benchmark to quantitatively measure the impact of the proposed collaborative scheme. We show in Table 2 qualitative results on the test sets of the RealBlur datasets composed of 980 blurry/sharp image pairs. We run UNet and UNet-T by splitting 512×512 random crops from the training set into a unique stack of size N in $\{1, 4, 16\}$ with 25% of overlap to take into

Location	Method	16mm f/2.8	24mm f/1.4	Params
Corner	UNet-TX ($N = 1$)	30.58 (-0.44)	32.83 (-0.58)	270K
Corner	UNet-TX ($N = 4, M$)	31.02	33.45	284K
Corner	UNet-TS ($N = 1$)	31.60 (-0.22)	34.10 (-0.47)	1.1M
Corner	UNet-TS ($N = 4, M$)	31.82	34.57	1.1M
Corner	UNet-T ($N = 1$)	32.21 (-0.06)	34.88 (-0.35)	4.3M
Corner	UNet-T ($N = 4, M$)	32.27	35.32	4.6M
Intermediate	UNet-TX ($N = 1$)	34.45 (-0.34)	34.89 (-0.14)	270K
Intermediate	UNet-TX ($N = 4, M$)	34.79	35.03	284K
Intermediate	UNet-TS ($N = 1$)	35.12 (-0.37)	35.55 (-0.18)	1.1M
Intermediate	UNet-TS ($N = 4, M$)	35.49	35.73	1.1M
Intermediate	UNet-T ($N = 1$)	35.89 (-0.23)	36.22 (-0.01)	4.3M
Intermediate	UNet-T ($N = 4, M$)	36.12	36.23	4.6M
Center	UNet-TX ($N = 1$)	36.94 (-0.57)	36.71 (-0.21)	270K
Center	UNet-TX ($N = 4, M$)	37.57	36.92	284K
Center	UNet-TS ($N = 1$)	38.02 (-0.36)	37.93 (-0.03)	1.1M
Center	UNet-TS ($N = 4, M$)	38.38	37.96	1.1M
Center	UNet-T ($N = 1$)	39.10 (-0.18)	38.99 (-0.00)	4.3M
Center	UNet-T ($N = 4, M$)	39.28	38.99	4.6M

Table 3: Optical aberration removal for two lenses calibrated in [5]. The PSNR is reported from three different locations on the field of view. The difference between using 1 or 4 images is shown in parenthesis. Setting N to 4 helps compensating the reduction of the width and parameters.

account the patches will be stitched back into a full-sized image for evaluation with the protocol of [38]. During training, we supervise each patch of the stack with the corresponding patch in the target with the loss (4). At test time, we start from the full image, slice it into N patches, and stitch together the predicted sharps variants into a full sharp estimate with the same windowing approach as in [39]. We benchmark different choices of pooling layer p : max (M), lambda (L) and SA (A). We use the same training strategy as MIMOUNet and also retrain the latter for fair comparison: We train for 1k epochs with the Adam optimizer with initial learning rate set to 0.0001 and decayed by 0.5 every 200 epoch. The batch size is set to 8. We see that increasing the stack size N within the *same* patch and more refined pooling p benefit the deblurring accuracy for all metrics when using a UNet not initially designed for deblurring, in contrast to [40] and [10]. For instance Remark a 17M-parameter Unet cannot beat MIMOUNet [10], but after being upgraded, the performances are boosted by at margins up to +1.33dB. UNet-T with p implemented with SA and $N = 16$ notably cope with MIMONet with less parameters. We also observe that both refining p and increasing N increase the performance of UNet, validating our strategy. An example is shown in Figure 4.

Optical aberrations. We leverage the near central symmetry of aberrations around the optical center of the lens [39] by sampling at $N = 4$ locations on the field of view, one for each quadrant of the Cartesian plane, (see Figure 2). Since no real-world pairs of aberrated and aberration-free image dataset exists, we generate synthetic data from two of the 70 PSFs calibrated in [5]. Each PSF consists of about 4,000 local RGB kernels accounting for both monochromatic and chromatic aberrations. We select the Canon EF16-35mm f/2.8L USM EI at shortest focal length and maximal aperture and the Canon EF24mm f/1.4L USM that are prone to aberrations after visual inspection, the former being poorer than the latter. We convert from JPEG to pseudo-linear RGB images the 128×128 patches from the DIV2K images with the protocol of [7], and blur each color channel with the corresponding one from local filters sampled at random in the given PSF. We add 0.5/255 Gaussian noise to account for noise residual after demosaicking in an ISP pipeline. We train for each PSF, UNet-T, UNet-TS and UNet-TX for $N = 1$ and $N = 4$ with max pooling as collaborative strategy since in an ISP pipeline within a handheld camera, each module should be as lightweight as possible. We train for 500k iterations with the Adam optimizer with batch size of 16, and an initial learning rate of 10^{-4} decayed by 0.2 after 200k and 400k iterations. Table 3 shows the PSNR for three locations on the lens field-of-view with growing loss of quality from the center to a corner. For both lenses the collaborative variant is always above the model with $N = 1$ with significant margins

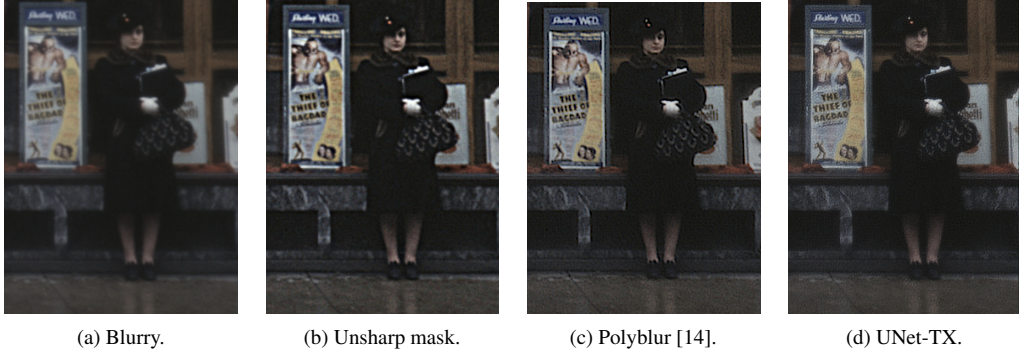


Figure 5: Sharpening on the heritage image from [39]. The two classical methods have hyper-parameters to tune whereas our UNet-TX with $N = 8$ has not and produce a halo-free sharp result.

between +0.2 and +0.6dB for UNet-TX. We observe more important improvements for the 16mm lens than the 24mm. Since the former is a zoom lens, it has in average a poorer quality than a prime lens, thus benefiting more from collaboration, especially for UNet-TX, validating the assumption that collaboration helps to design practical lightweight networks. We can reasonably expect that on devices with worse optical quality like smartphones, collaboration may help even further.

Sharpening. In the absence of any benchmark evaluating sharpening algorithms, we simply run a qualitative comparison for sharpening. Since mild blurs may be reasonably approximated with Gaussians [17], we select the lightweight UNet-TX trained in Section 5.2 and compare it with Polyblur [14] and the unsharp mask algorithm, two approaches used on-device, for instance to postprocess multi-frame algorithms like in the context of super-resolution or high-dynamic range imaging [28]. The comparison is run on a heritage photograph from [39], and shown in Figure 5.

Discussion and limitations. We have shown that the hypothesis that similar blurs exist in blurry images and may be gathered is verified, and leads to improvements in each situation. Second, these improvements are obtained for a learning-free max pooling layer that leads to lightweight efficient models for sharpening and optical aberration correction. In these cases, $N = 4$ or $N = 8$ similar patches are enough. For more diverse blur families such as camera shake, learning-based pooling strategies and more important stack sizes, *e.g.*, $N = 16$ instead of 4, lead to significant boost, suggesting that in this case, the more patches and pooling capacity, the better.

Nevertheless the proposed approach has limits. Finding patches with similar blurs is not straightforward when the blur may vary non-continuously, in particular with segmentation-aware blurs such as the dynamic blur featured in the GoPro dataset [33], or depth-dependent defocus blur [21]. Another problem may arise if not enough patches with the same blur are collected. We remarked during our experiments that important noise alters the collaboration, thus limiting the benefits of our approach in high-noise regimes. Yet, deblurring in such regime is an objective [4] beyond the scope of this paper. We have shown that for three realistic blurring scenarios our method was effective.

6 Conclusion

In this paper, we have presented a simple modification of existing CNNs for enhanced blind image deblurring. It consists in processing together images with the same latent blur to share the different features of the blur across the images within a network which has internal collaborative layers taking the form of feature maps pooling. Finding several images having similar latent blurs is verified to be possible for a wide range of practical single-image blind deblurring applications. Experiments on both synthetic and real-world images covering camera shake removal, optical aberration compensation and sharpening validate our approach and highlight the versatility of possible collaborating layers to design efficient models. This seems to establish a practical framework upon which building both lightweight and state-of-the-art architectures.

Aknowledgemnts. This work was partly financed by the DGA Astrid Maturation project SURE-CAVI ANR-21-ASM3-0002, the Office of Naval research grant N00014-17-1-2552, and the ANR project IMPROVED ANR-22-CE39-0006-04. This work was performed using HPC resources from GENCI-IDRIS (grants 2023-AD011012453R2, 2023-AD011012458R2). Centre Borelli is also with Université Paris Cité, SSA and INSERM. The authors thank Adrien Courtois for fruitful discussions and help with the learnable pooling layers’ implementations.

References

- [1] Abdullah Abuolaim and Michael S. Brown. Defocus deblurring using dual-pixel data. In *European Conference on Computer Vision*, pages 111–126. Springer, 2020.
- [2] Eirikur Agustsson and Radu Timofte. NTIRE 2017 challenge on single image super-resolution: Dataset and study. In *IEEE Conference on Computer Vision and Pattern Recognition Workshops*, pages 1122–1131, 2017.
- [3] Miika Aittala and Frédo Durand. Burst image deblurring using permutation invariant convolutional neural networks. In *European Conference on Computer Vision*, pages 748–764. Springer, 2018.
- [4] Jérémy Anger, Gabriele Facciolo, and Mauricio Delbracio. Blind image deblurring using the ℓ_0 gradient prior. *Image Processing On Line*, 9:124–142, 2019.
- [5] Matthias Bauer, Valentin Volchkov, Michael Hirsch, and Bernhard Schölkopf. Automatic estimation of modulation transfer functions. In *IEEE International Conference on Computational Photography*, pages 1–12, 2018.
- [6] Irwan Bello. LambdaNetworks: Modeling long-range interactions without attention. In *International Conference on Learning Representations*, pages 1–14. OpenReview.net, 2021.
- [7] Tim Brooks, Ben Mildenhall, Tianfan Xue, Jiawen Chen, Dillon Sharlet, and Jonathan T. Barron. Un-processing images for learned raw denoising. In *IEEE/CVF Conference on Computer Vision and Pattern Recognition*, pages 11036–11045, 2019.
- [8] Mo Chen, Jessica Fridrich, Miroslav Goljan, and Jan Lukás. Determining image origin and integrity using sensor noise. *IEEE Transactions on information forensics and security*, 3(1):74–90, 2008.
- [9] Shiqi Chen, Huajun Feng, Dexin Pan, Zhihai Xu, Qi Li, and Yue-ting Chen. Optical aberrations correction in postprocessing using imaging simulation. *ACM Transactions on Graphics*, 40(5):192:1–192:15, 2021.
- [10] Sung-Jin Cho, Seo-Won Ji, Jun-Pyo Hong, Seung-Won Jung, and Sung-Jea Ko. Rethinking coarse-to-fine approach in single image deblurring. In *IEEE/CVF International Conference on Computer Vision*, pages 4621–4630, 2021.
- [11] Xiaojie Chu, Liangyu Chen, Chengpeng Chen, and Xin Lu. Improving image restoration by revisiting global information aggregation. In *European Conference on Computer Vision*, pages 53–71. Springer, 2022.
- [12] Florent Couzinie-Devy, Jian Sun, Karteek Alahari, and Jean Ponce. Learning to estimate and remove non-uniform image blur. In *IEEE Conference on Computer Vision and Pattern Recognition*, pages 1075–1082, 2013.
- [13] Kostadin Dabov, Alessandro Foi, Vladimir Katkovnik, and Karen O. Egiazarian. Image denoising by sparse 3-D transform-domain collaborative filtering. *IEEE Transactions on Image Processing*, 16(8):2080–2095, 2007.
- [14] Mauricio Delbracio, Ignacio Garcia-Dorado, Sungjoon Choi, Damien Kelly, and Peyman Milanfar. Poly-blur: Removing mild blur by polynomial reblurring. *IEEE Transactions on Computational Imaging*, 7:837–848, 2021.
- [15] Mauricio Delbracio and Peyman Milanfar. Inversion by direct iteration: An alternative to denoising diffusion for image restoration. *arXiv preprint arXiv:2303.11435*, 2023.
- [16] Mauricio Delbracio and Guillermo Sapiro. Removing camera shake via weighted Fourier burst accumulation. *IEEE Transactions on Image Processing*, 24(11):3293–3307, 2015.
- [17] Thomas Eboli, Jean-Michel Morel, and Gabriele Facciolo. Breaking down polyblur: Fast blind correction of small anisotropic blurs. *Image Processing On Line*, 12:435–456, 2022.

- [18] Thomas Eboli, Jean-Michel Morel, and Gabriele Facciolo. Fast two-step blind optical aberration correction. In *European Conference on Computer Vision*, pages 693–708. Springer, 2022.
- [19] Hongyun Gao, Xin Tao, Xiaoyong Shen, and Jiaya Jia. Dynamic scene deblurring with parameter selective sharing and nested skip connections. In *IEEE/CVF Conference on Computer Vision and Pattern Recognition*, pages 3848–3856, 2019.
- [20] Amit Goldstein and Raanan Fattal. Blur-kernel estimation from spectral irregularities. In *European Conference on Computer Vision*, pages 622–635. Springer, 2012.
- [21] Samuel W. Hasinoff and Kiriakos N. Kutulakos. A layer-based restoration framework for variable-aperture photography. In *IEEE International Conference on Computer Vision*, pages 1–8, 2007.
- [22] Zhe Hu and Ming-Hsuan Yang. Learning good regions to deblur images. *International Journal on Computer Vision*, 115(3):345–362, 2015.
- [23] Eric Kee, Sylvain Paris, Simon Chen, and Jue Wang. Modeling and removing spatially-varying optical blur. In *IEEE International Conference on Computational Photography*, pages 1–8, 2011.
- [24] Orest Kupyn, Tetiana Martyniuk, Junru Wu, and Zhangyang Wang. DeblurGAN-v2: Deblurring (orders-of-magnitude) faster and better. In *IEEE/CVF International Conference on Computer Vision*, pages 8877–8886, 2019.
- [25] Jamy Lafenetre, Gabriele Facciolo, and Thomas Eboli. Implementing handheld burst super-resolution. *Image Processing On Line*, 13, 2023.
- [26] Wei-Sheng Lai, Yichang Shih, Lun-Cheng Chu, Xiaotong Wu, Sung-Fang Tsai, Michael Krainin, Deqing Sun, and Chia-Kai Liang. Face deblurring using dual camera fusion on mobile phones. *ACM Transactions on Graphics*, 41(4):148:1–148:16, 2022.
- [27] Jean-François Lalonde, Srinivasa G Narasimhan, and Alexei A Efros. What do the sun and the sky tell us about the camera? *International Journal of Computer Vision*, 88(1):24–51, 2010.
- [28] Bruno Lecouat, Thomas Eboli, Jean Ponce, and Julien Mairal. High dynamic range and super-resolution from raw image bursts. *ACM Transactions on Graphics*, 41(4):38:1–38:21, 2022.
- [29] Anat Levin, Yair Weiss, Frédo Durand, and William T. Freeman. Understanding and evaluating blind deconvolution algorithms. In *IEEE Conference on Computer Vision and Pattern Recognition*, pages 1964–1971, 2009.
- [30] Ze Liu, Yutong Lin, Yue Cao, Han Hu, Yixuan Wei, Zheng Zhang, Stephen Lin, and Baining Guo. Swin transformer: Hierarchical vision transformer using shifted windows. In *IEEE/CVF International Conference on Computer Vision*, pages 9992–10002, 2021.
- [31] Karima Ma, Michaël Gharbi, Andrew Adams, Shoaib Kamil, Tzu-Mao Li, Connelly Barnes, and Jonathan Ragan-Kelley. Searching for fast demosaicking algorithms. *ACM Transactions on Graphics*, 41(5):172:1–172:18, 2022.
- [32] Tomer Michaeli and Michal Irani. Blind deblurring using internal patch recurrence. In *European Conference on Computer Vision*, pages 783–798. Springer, 2014.
- [33] Seungjun Nah, Tae Hyun Kim, and Kyoung Mu Lee. Deep multi-scale convolutional neural network for dynamic scene deblurring. In *IEEE Conference on Computer Vision and Pattern Recognition*, pages 257–265, 2017.
- [34] Jinshan Pan, Deqing Sun, Hanspeter Pfister, and Ming-Hsuan Yang. Deblurring images via dark channel prior. *IEEE Transactions on Pattern Analysis and Machine Intelligence*, 40(10):2315–2328, 2018.
- [35] Dongwon Park, Dong Un Kang, Jisoo Kim, and Se Young Chun. Multi-temporal recurrent neural networks for progressive non-uniform single image deblurring with incremental temporal training. In *European Conference on Computer Vision*, pages 327–343. Springer, 2020.
- [36] Sung Hee Park and Marc Levoy. Gyro-based multi-image deconvolution for removing handshake blur. In *IEEE Conference on Computer Vision and Pattern Recognition*, pages 3366–3373, 2014.
- [37] René Ranftl, Alexey Bochkovskiy, and Vladlen Koltun. Vision transformers for dense prediction. In *IEEE/CVF International Conference on Computer Vision*, pages 12159–12168, 2021.

- [38] Jaesung Rim, Haeyun Lee, Jucheol Won, and Sunghyun Cho. Real-world blur dataset for learning and benchmarking deblurring algorithms. In *European Conference on Computer Vision*, pages 184–201. Springer, 2020.
- [39] Christian J. Schuler, Michael Hirsch, Stefan Harmeling, and Bernhard Schölkopf. Blind correction of optical aberrations. In *European Conference on Computer Vision*, pages 187–200. Springer, 2012.
- [40] Xin Tao, Hongyun Gao, Xiaoyong Shen, Jue Wang, and Jiaya Jia. Scale-recurrent network for deep image deblurring. In *IEEE Conference on Computer Vision and Pattern Recognition*, pages 8174–8182, 2018.
- [41] Ashish Vaswani, Noam Shazeer, Niki Parmar, Jakob Uszkoreit, Llion Jones, Aidan N. Gomez, Lukasz Kaiser, and Illia Polosukhin. Attention is all you need. In *Advances in Neural Information Processing Systems*, pages 5998–6008, 2017.
- [42] Zhendong Wang, Xiaodong Cun, Jianmin Bao, Wengang Zhou, Jianzhuang Liu, and Houqiang Li. Uformer: A general U-shaped transformer for image restoration. In *IEEE/CVF Conference on Computer Vision and Pattern Recognition*, pages 17662–17672, 2022.
- [43] Jay Whang, Mauricio Delbracio, Hossein Talebi, Chitwan Saharia, Alexandros G. Dimakis, and Peyman Milanfar. Deblurring via stochastic refinement. In *IEEE/CVF Conference on Computer Vision and Pattern Recognition*, pages 16272–16282, 2022.
- [44] Oliver Whyte, Josef Sivic, Andrew Zisserman, and Jean Ponce. Non-uniform deblurring for shaken images. *International Journal on Computer Vision*, 98(2):168–186, 2012.
- [45] Li Xu, Shicheng Zheng, and Jiaya Jia. Unnatural L_0 sparse representation for natural image deblurring. In *IEEE Conference on Computer Vision and Pattern Recognition*, pages 1107–1114, 2013.
- [46] Zhengyou Zhang. A flexible new technique for camera calibration. *IEEE Transactions on Pattern Analysis and Machine Intelligence*, 22(11):1330–1334, 2000.

A Broader impact

The proposed technique aims at improving blind image deblurring. We are aware that image processing may be used for non-ethical goals such as face recognition. However, we believe that the technology is not mature enough to be used as is in a surveillance system for instance, and is thus not harmful. We however think it can be useful for personal photography or certain scientific fields where imagery plays a key role.

B Training details

We provide in this section additional details on the training protocols of all the tasks and all the quantitative results for all experiments: PSNR, SSIM and LPIPS.

B.1 Pooling layer p implementations

We detail in the main paper three approaches to implement the pooling function p in Eq. (5): max pooling, lambda layer [6] and the self-attention module [41]. We provide formal definitions of these layers below. We recall Equations (5) and (6) in the main paper:

$$g = p(\{e_1, \dots, e_N\}), \quad (7)$$

and

$$e_n \leftarrow \text{conv}_{1 \times 1}(\{e_n, g\}), \quad \forall n \in \{1, \dots, N\}. \quad (8)$$

For the sake of explanation in this part, each feature map e_n ($n = 1, \dots, N$) and the global feature map g have dimension $H \times W \times C$. We provide in what follows the python codes of our pooling modules. In all the codes we provide, the output array g is of shape (BN, C, H, W) . The additional N shape is for merging in a batch manner g with the N intermediate feature vectors within the subsequent 1×1 convolutions layers. We first need in preamble of these codes a few standard layers:

Algorithm 1: Layer Norm and Layer Scale layers.

```
def _pad_as(x, ref):
    _, _, *dims = ref.size()

    for _ in range(len(dims)):
        x = x.unsqueeze(dim=-1)

    return x

class LayerNorm(nn.Module):
    def __init__(self, in_channels: int, eps: float = 1e-6) -> None:
        super().__init__()

        self.eps = eps
        self.weight = nn.Parameter(torch.ones(in_channels))
        self.bias = nn.Parameter(torch.zeros(in_channels))

    def forward(self, x: torch.Tensor) -> torch.Tensor:
        u = x.mean(1, keepdim=True)
        s = (x - u).pow(2).mean(1, keepdim=True)
        x = (x - u) / torch.sqrt(s + self.eps)

        return torch.einsum("c, b c ... -> b c ...", self.weight, x) + _pad_as(self.bias, x)

class LayerScale(nn.Module):
    def __init__(self, in_channels: int, init: Optional[float] = 0.1):
        super().__init__()

        self.init = init
```

```

    if init is not None:
        self.weight = nn.Parameter(init * torch.ones(in_channels))

def forward(self, x):
    if self.init is not None:
        return torch.einsum("b c ..., c -> b c ...", x, self.weight)

    return x

```

Max pooling. As in [3], we may simply implement p as an entrywise max operation.

Algorithm 2: Max pooling module

```

class PixelwiseMax(nn.Module):
    def __init__(self, N: int) -> None:
        super().__init__()

        self.N = N

    def forward(self, x: torch.Tensor) -> torch.Tensor:
        """
        Input: torch.Tensor of dimension [B * N, C, H, W]
        Output: torch.Tensor of dimension [B * N, C, H, W]
        """

        BN, C, H, W = x.size() # (BN,C,H,W)
        B = BN // self.N

        # Pooling on the stack N axis.
        x_ = x.reshape(B, -1, C, H, W)
        g, _ = torch.max(x_, dim=1, keepdim=True) # (B,1,C,H,W)
        g = g.repeat(1, self.N, 1, 1, 1).reshape(BN,C,H,W)

    return g

```

Self-attention module [41]. We may implement the self-attention mechanism as defined in [41] to propose a learning-based variant to the max pooling that finds interesting information to extract from a sequence of feature maps.

Algorithm 3: Self-attention pooling module

```

class PixelwiseSAUp(nn.Module):
    def __init__(self, in_channels: int, N: int, heads: Optional[int] = None,
                 layerscale_init: Optional[float] = 0.1) -> None:
        super().__init__()

        self.N = N
        self.heads = heads or in_channels // 32

        self.prenorm = LayerNorm(in_channels)
        self.to_QKV = nn.Conv2d(in_channels, 3 * in_channels, 1)
        self.layerscale = LayerScale(in_channels, init=layerscale_init)

        self.mlp = nn.Sequential(
            LayerNorm(in_channels),
            nn.Conv2d(in_channels, 4 * in_channels, 1),
            nn.GELU(),
            nn.Conv2d(4 * in_channels, in_channels, 1),
            LayerScale(in_channels, init=layerscale_init)
        )

    def forward(self, x: torch.Tensor) -> torch.Tensor:
        """
        Input: torch.Tensor of dimension [B * N, C, H, W]

```

```

Output: torch.Tensor of dimension [B * N, C, H, W]
"""

BN, C, H, W = x.size()
B = BN // self.N

# Query-Key-Value decomposition.
QKV = self.to_QKV(self.prenorm(x))
Q, K, V = torch.chunk(QKV, 3, dim=1)
Q, K, V = map(lambda x: x.view(B, self.N, self.heads, -1, H, W), (Q, K, V))

# Generate attention matrix.
A = torch.einsum("b n h c i j, b m h c i j -> b n m h i j", Q, K)
A = A / sqrt(Q.size(3))
A = A.softmax(2)

# Apply the attention matrix.
g = torch.einsum("b n m h i j, b m h c i j -> b n h c i j", A, V)
g = g.reshape(BN, C, H, W)

# Refining MLP.
g = x + self.layerscale(g)
g = g + self.mlp(g)

return g

```

Lambda layer [6]. the Lambda layer as proposed in [6] is a sort of lightweight attention-like mechanism that is a valid candidate for implementing p . In the main paper for camera shake, we see in Table 2 that it leads to results better than max pooling and lower than SA, but for a smaller additional number of parameter.

Algorithm 4: Lambda pooling module

```

class PixelwiseLambdaUp(nn.Module):
    def __init__(self, in_channels: int, k: int, N: int, layerscale_init: Optional[float] = 0.1) -> None:
        super().__init__()

        self.N = N # Number of frames in the stack.
        self.k = k # Number of features in the Lambda layer.

        self.prenorm = LayerNorm(in_channels)
        self.to_K = nn.Conv2d(in_channels, k, 1)
        self.to_Q = nn.Conv2d(in_channels, in_channels, 1)
        self.merge_inner = nn.Conv2d((k + 1) * in_channels, in_channels, 1)
        self.layerscale = LayerScale(in_channels, init=layerscale_init)

    def forward(self, x: torch.Tensor) -> torch.Tensor:
        """
        Input: torch.Tensor of dimension [B * N, C, H, W]
        Output: torch.Tensor of dimension [B * N, C, H, W]
        """

        BN, _, H, W = x.size()
        B = BN // self.N

        # Query-Key decomposition on k features.
        x_norm = self.prenorm(x)
        Q = self.to_Q(x_norm)
        K = self.to_K(x_norm)
        Q, K = map(lambda x: x.view(B, self.N, -1, H, W), (Q, K))

        # Merge of the k features in a single array.
        K = K.softmax(1)
        output = torch.einsum('b n k i j, b n c i j -> b k c i j', K, Q)

```

```

# Concatenate output to input
output = output.reshape(B, 1, -1, H, W)
output = output.repeat(1, self.N, 1, 1, 1)
output = output.reshape(-1, output.size(2), H, W)

g = torch.cat((x, output), 1)
g = self.merge_inner(g)
g = self.layerscale(g)

return g

```

B.2 Architectures of UNet and UNet-T

We provide diagrams in Figures 6 and 7 of the considered UNet and UNet-T architectures respectively. To get the architectures of UNet-S and UNet-X, divide the channel widths shown in the Figure by 2 and 4 respectively. The same goes to get UNet-TS and UNet-TX from UNet-T. We have not exhaustively searched for an efficient architecture. Other configurations embedding the pooling layer may lead to better or worse results. When $N = 1$, the pooling module (gray box) in Figures 6 and 7 is removed, yielding a classical UNet merging the contributions of the upsampled features and the ones in the encoder at the same scale.

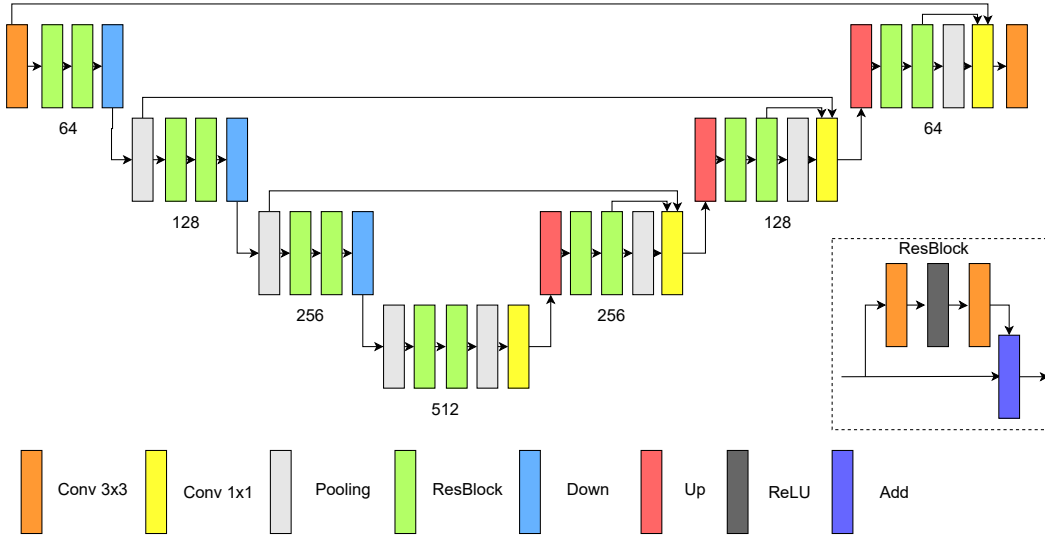


Figure 6: Diagram of UNet.

B.3 Slicing the images per type of blur

Camera shake. We focus on the Realblur-J [38] images that are roughly of size 700×700 . When we restore an image of the test set (like in Table 2), we simply slice the image into overlapping patches with 25% of overlap. Empirically, we have noticed that since the images are downsampled versions of 12Mp photographs, each patch has a sufficient different content from the other ones. In the draft, we have limited ourselves to $N = 1, 4$ or 16 but in practice even more patches may be considered.

Sharpening. We follow the same strategy as for camera shake since the blur that should be removed by a sharpening stage such as fusion blur [17] or mild blur [14] are a sort of Gaussian blur that is similar across the image field of view. We thus first slice the image into overlapping patches with overlap of 25%. We then feed stacks of N patches to the model, and when all the patches have been processed by stack, we rearrange the patches into the full image with the Bartlett window to eliminate the fusion artifacts [39].

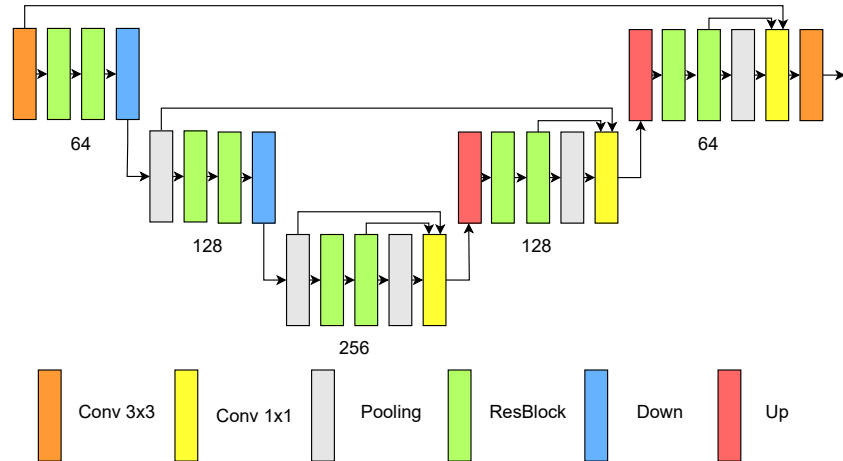


Figure 7: Diagram of UNet-T.

Optical aberration. Most images where optical aberration should be removed are either raw images in 12, 24 or even 60Mpixel resolution [5, 18], are large-enough JPEG images where the aberrations are visible [23, 39]. Patch slicing is thus a viable strategy to handle the size of the images and the non-uniformness of the blur [9, 18].

When provided an aberrated image, we select the patches in the top-left quadrant of the image with respect of the optical center, and select the three corresponding crops with respect to the horizontal and vertical symmetries. Other symmetries could be exploited like diagonal symmetries but we have not explored that direction.

B.4 Training protocols

For the sake of reproducibility, we present here all the the training details that may have not fit into the main paper.

Gaussian blur. We select the 800 training images of the DIV2K dataset [2]. We randomly crop 128×128 RGB patches from these images, unprocess them with the protocol of [7] (inverse tone mapping, gamma expansion, and inverse color matrix), blur the images with Gaussian blurs with standard deviations along the two principal axes in $[0.3, 4]^2$ and orientation randomly sampled in $[0, 2\pi]$, add Gaussian noise with standard deviation in $[0.5, 2]/255$. We then reprocess the image (color matrix, gamma compression, and tone mapping). This mimics that RGB images are generally shown in a domain where the blur kernel has not a simple linear relationship with the blurry image at end because of a camera ISP.

For each training stack of size N , we randomly select a single Gaussian blur and noise level, and an image among the 800 at hand from which we crop N patches in it, and degrade them with the protocol shown above to generate the input stack of N blurry images sharing the same blur.

Optical aberration. We follow the same strategy as for Gaussian blur, but do not reapply the camera color matrix, gamma compression and tone mapping to be in a case where the correction is applied on a linear RGB image since optical aberration correction is one of the core tasks of an ISP pipeline [18].

Because of how are sampled the patches in a real aberrated images (cf Section B.3), we restrict the number of images N in the stack to be either 1 or 4. For $N = 1$ and the given PSF chosen among the 70 from [5], we uniformly sample a location on the field of view of the camera and select the nearest local 41×41 RGB filter. It is applied to the 128×128 RGB random crop. For $N = 4$, we instead sample a location in the top-left quadrant of the field of view of the camera, and fetch the 4 local RGB filters following the vertical and horizontal symmetry. These local RGB filters are all *similar* but not exactly the same, thus training our model to handle the differences of support.

Camera shake. For camera shake removal in the Realblur-J dataset [38], we select an image, uniformly sample a 256×256 crop and slice into into $N = 4$ or $N = 16$ *non-overlapping* patches of the same size, *i.e.*, 4 patches of size 128×128 or 16 patches of size 64×64 . The rationale behind this choice is that we simply want to learn deblurring, not deblurring an image like at test time. We found that this simple and fast strategy was working well in practice since the estimated blur kernels provided with the dataset are almost all of support smaller than 54×64 pixels, thus for all values of N , the patches capture the whole support of the blur.

C Additional quantitative results

We provide in this section the results for the three metrics PSNR, SSIM and LPIPS to complement the Tables 1 and 3, and Figure 3 where we present results only for the average PSNR because of lack of space.

C.1 Gaussian blur (depth)

The following tables complement Table 1 in the main paper where we reported only the average PSNR over 3 splits of the dataset. We show in Tables 4, 5 and 6 the average PSNR, SSIM and LPIPS scores for the 100 DIV2K test images used to evaluate the different models, per stack size N and standard deviation of the isotropic Gaussian blur σ . The average PSNR scores are those shown in Table 1 in the main paper. On the three metrics one may observe improvements with N , and saturation happening around $N = 8$, as noted in the main paper.

	σ	1	2	3	4	Average
UNet-T	$N = 1$	35.59	32.67	31.25	30.35	32.46
UNet-T	$N = 2$	36.05	33.04	31.44	30.46	32.75
UNet-T	$N = 4$	36.31	33.20	31.56	30.58	32.92
UNet-T	$N = 8$	36.70	33.44	31.73	30.66	33.13
UNet-T	$N = 16$	36.59	33.34	31.59	30.45	33.02
UNet	$N = 1$	35.97	33.01	31.41	30.61	32.75
UNet	$N = 2$	36.43	33.33	31.55	30.64	32.99
UNet	$N = 4$	36.51	33.46	31.64	30.70	33.08
UNet	$N = 8$	36.62	33.51	31.76	30.71	33.15
UNet	$N = 16$	36.51	33.46	31.53	30.48	33.07

Table 4: PSNR scores for UNet and UNet-T per standard deviation level σ , and with p implemented with max pooling.

	σ	1	2	3	4	Average
UNet-T	$N = 1$	0.960	0.923	0.896	0.859	0.910
UNet-T	$N = 2$	0.961	0.926	0.898	0.873	0.915
UNet-T	$N = 4$	0.963	0.928	0.899	0.876	0.917
UNet-T	$N = 8$	0.965	0.930	0.902	0.878	0.919
UNet-T	$N = 16$	0.964	0.929	0.900	0.875	0.918
UNet	$N = 1$	0.962	0.926	0.898	0.876	0.916
UNet	$N = 2$	0.963	0.928	0.899	0.877	0.917
UNet	$N = 4$	0.964	0.930	0.900	0.878	0.918
UNet	$N = 8$	0.964	0.930	0.902	0.879	0.919
UNet	$N = 16$	0.964	0.928	0.900	0.878	0.918

Table 5: SSIM scores for UNet and UNet-T per standard deviation level σ , and with p implemented with max pooling.

	σ	1	2	3	4	Average
UNet-T	$N = 1$	0.029	0.075	0.120	0.159	0.096
UNet-T	$N = 2$	0.026	0.069	0.115	0.152	0.091
UNet-T	$N = 4$	0.021	0.064	0.112	0.146	0.086
UNet-T	$N = 8$	0.015	0.058	0.107	0.140	0.080
UNet-T	$N = 16$	0.016	0.059	0.108	0.142	0.081
UNet	$N = 1$	0.025	0.068	0.113	0.145	0.088
UNet	$N = 2$	0.022	0.063	0.110	0.142	0.084
UNet	$N = 4$	0.021	0.060	0.108	0.136	0.081
UNet	$N = 8$	0.017	0.058	0.105	0.135	0.079
UNet	$N = 16$	0.016	0.060	0.109	0.141	0.081

Table 6: LPIPS scores for UNet and UNet-T per standard deviation level σ , and with p implemented with max pooling.

C.2 Gaussian blur (width)

The following tables complement Figure 3 in the main paper where we reported only the average PSNR over 3 splits of the dataset. We show in Tables 4, 5 and 6 the average PSNR, SSIM and LPIPS scores for the 100 DIV2K test images used to evaluate the different models, per stack size N and standard deviation of the isotropic Gaussian blur σ . The average PSNR scores are those shown in Figure 3 in the main paper. For each width, the variant with $N = 8$ achieves better results than the counterpart with $N = 1$, especially σ set to 1 and 2, typical values for image sharpening [17].

Notably, the performance of UNet-TX ($N = 8$) is similar to that of UNet-TS ($N = 1$), and the performance of UNet-TS ($N = 8$) is superior to that of UNet ($N = 1$), despite the first models being four times smaller than the second ones. This is true for all three metrics, and thus validates our claim that collaborative filtering helps miniaturizing deblurring networks.

	σ	1	2	3	4	Average
UNet-TX	$N = 1$	33.84	31.80	30.70	29.43	31.44
UNet-TX	$N = 8$	34.63	32.25	30.81	29.80	31.87
UNet-TS	$N = 1$	34.86	32.32	31.10	29.88	32.04
UNet-TS	$N = 8$	35.80	33.03	31.40	30.36	32.65
UNet-T	$N = 1$	35.59	32.67	31.25	30.35	32.47
UNet-T	$N = 8$	36.70	33.43	31.73	30.66	33.13
UNet-X	$N = 1$	34.22	32.04	30.83	29.79	31.72
UNet-X	$N = 8$	35.01	32.53	31.03	30.03	32.15
UNet-S	$N = 1$	35.34	32.65	31.21	30.30	32.38
UNet-S	$N = 8$	35.99	33.21	31.55	30.47	32.81
UNet	$N = 1$	35.97	33.01	31.41	30.61	32.75
UNet	$N = 8$	36.62	33.51	31.76	30.71	33.15

Table 7: Average PSNR to benchmark width of the models.

C.3 Optical aberration

We report the PSNR, SSIM and LPIPS for the two lenses benchmarked in Table 3 in the main paper. The results for the 16mm lens are in Table 10 and those of the 24mm lens are reported in Table 11. We run the models on 3 different sets of patches to compute error bars on the variety of sets of patches that may be collected in practice. However in the main paper we only run the methods on a single arrangement of the image patches (explaining the slight differences of average PSNRs). The differences between $N = 1$ and $N = 4$ in these tables and Table 3 in the main paper are approximately of the same order. The error bar reported in Tables 10 and 11 are the standard deviation of the metrics on the three runs.

	σ	1	2	3	4	Average
UNet-TX	$N = 1$	0.946	0.912	0.886	0.851	0.899
UNet-TX	$N = 8$	0.951	0.917	0.889	0.862	0.905
UNet-TS	$N = 1$	0.954	0.919	0.892	0.860	0.906
UNet-TS	$N = 8$	0.960	0.926	0.897	0.873	0.914
UNet-T	$N = 1$	0.960	0.923	0.896	0.869	0.912
UNet-T	$N = 8$	0.965	0.930	0.902	0.878	0.919
UNet-X	$N = 1$	0.948	0.915	0.889	0.861	0.903
UNet-X	$N = 8$	0.954	0.920	0.891	0.867	0.908
UNet-S	$N = 1$	0.958	0.923	0.895	0.870	0.912
UNet-S	$N = 8$	0.960	0.927	0.899	0.876	0.916
UNet	$N = 1$	0.962	0.926	0.898	0.876	0.916
UNet	$N = 8$	0.964	0.930	0.902	0.879	0.919

Table 8: Average SSIM to benchmark width of the models.

	σ	1	2	3	4	Average
UNet-TX	$N = 1$	0.043	0.093	0.140	0.191	0.117
UNet-TX	$N = 8$	0.031	0.077	0.123	0.162	0.098
UNet-TS	$N = 1$	0.037	0.084	0.129	0.178	0.107
UNet-TS	$N = 8$	0.020	0.063	0.113	0.149	0.086
UNet-T	$N = 1$	0.029	0.075	0.120	0.159	0.096
UNet-T	$N = 8$	0.015	0.058	0.107	0.140	0.080
UNet-X	$N = 1$	0.038	0.082	0.126	0.172	0.105
UNet-X	$N = 8$	0.026	0.069	0.116	0.151	0.091
UNet-S	$N = 1$	0.028	0.074	0.119	0.156	0.094
UNet-S	$N = 8$	0.019	0.061	0.109	0.143	0.083
UNet	$N = 1$	0.025	0.068	0.113	0.145	0.088
UNet	$N = 8$	0.017	0.058	0.105	0.138	0.079

Table 9: Average LPIPS to benchmark width of the models.

We remark that the collaborative strategy is particularly efficient for the 16mm lens that is of less quality than the 24mm one. This suggests that for lower-quality lenses, collaboration is further helpful.

D Additional qualitative results

D.1 Sharpening

We provide an additional sharpening example from the two by-default images of the online super-resolution demo from [25]. We compare to the unsharp mask technique (classical technique for sharpening), and Polyblur [14] (state-of-the-art for learning-free image sharpening). Since the official implementation is not available, we use the non-official one powering the online demo [17]. The examples are shown in Figures 8 and 9. In general, our model does not suffer from halo artifacts like unsharp mask, and has no hyper-parameter to adjust like Polyblur to work well. Our images may lack a bit of contrast enhancement because we target Gaussian deblurring, a slightly different problem to sharpening that also seeks to improve the general contrast of the image.

D.2 Camera shake

We provide additional crops from the Realblur-J dataset [38]. We make N crops collaborating with the protocol described in the main paper: we slice the image into N overlapping patches with 25% of overlap to prevent fusion artifacts when building back the full-sized image with the technique of [39]. We show two results in Figures 10 and 11 where we illustrate the gradual positive impact

Location	Method	PSNR	SSIM	LPIPS
Corner	UNet-TX ($N = 1$)	30.78 ± 0.12	0.814 ± 0.003	0.223 ± 0.003
Corner	UNet-TX ($N = 4, M$)	31.21 ± 0.11	0.826 ± 0.003	0.214 ± 0.003
Corner	UNet-TS ($N = 1$)	31.76 ± 0.12	0.840 ± 0.003	0.196 ± 0.003
Corner	UNet-TS ($N = 4, M$)	32.01 ± 0.11	0.846 ± 0.003	0.186 ± 0.003
Corner	UNet-T ($N = 1$)	32.66 ± 0.12	0.861 ± 0.002	0.166 ± 0.003
Corner	UNet-T ($N = 4, M$)	32.86 ± 0.12	0.864 ± 0.002	0.164 ± 0.003
Intermediate	UNet-TX ($N = 1$)	34.54 ± 0.08	0.906 ± 0.001	0.108 ± 0.002
Intermediate	UNet-TX ($N = 4, M$)	34.92 ± 0.11	0.911 ± 0.001	0.105 ± 0.002
Intermediate	UNet-TS ($N = 1$)	35.29 ± 0.01	0.917 ± 0.001	0.092 ± 0.002
Intermediate	UNet-TS ($N = 4, M$)	35.66 ± 0.11	0.921 ± 0.001	0.088 ± 0.002
Intermediate	UNet-T ($N = 1$)	36.03 ± 0.10	0.927 ± 0.001	0.078 ± 0.002
Intermediate	UNet-T ($N = 4, M$)	36.32 ± 0.10	0.929 ± 0.001	0.076 ± 0.002
Center	UNet-TX ($N = 1$)	37.13 ± 0.11	0.954 ± 0.001	0.037 ± 0.001
Center	UNet-TX ($N = 4, M$)	37.72 ± 0.10	0.956 ± 0.001	0.035 ± 0.001
Center	UNet-TS ($N = 1$)	38.22 ± 0.11	0.961 ± 0.001	0.028 ± 0.001
Center	UNet-TS ($N = 4, M$)	38.51 ± 0.09	0.961 ± 0.001	0.027 ± 0.001
Center	UNet-T ($N = 1$)	39.24 ± 0.11	0.966 ± 0.001	0.021 ± 0.001
Center	UNet-T ($N = 4, M$)	39.37 ± 0.09	0.966 ± 0.001	0.020 ± 0.001

Table 10: Quantitative results for the Canon 16-35mm f/2.8 EI USM lens opened at f/2.8 and at 16mm [5].

Location	Method	PSNR	SSIM	LPIPS
Corner	UNet-TX ($N = 1$)	33.13 ± 0.12	0.881 ± 0.002	0.132 ± 0.002
Corner	UNet-TX ($N = 4, M$)	33.61 ± 0.13	0.893 ± 0.002	0.120 ± 0.002
Corner	UNet-TS ($N = 1$)	34.26 ± 0.12	0.903 ± 0.002	0.101 ± 0.002
Corner	UNet-TS ($N = 4, M$)	34.77 ± 0.13	0.911 ± 0.002	0.092 ± 0.002
Corner	UNet-T ($N = 1$)	35.05 ± 0.13	0.916 ± 0.002	0.085 ± 0.002
Corner	UNet-T ($N = 4, M$)	35.47 ± 0.12	0.921 ± 0.001	0.082 ± 0.002
Intermediate	UNet-TX ($N = 1$)	35.08 ± 0.13	0.909 ± 0.002	0.107 ± 0.002
Intermediate	UNet-TX ($N = 4, M$)	35.22 ± 0.14	0.911 ± 0.002	0.105 ± 0.002
Intermediate	UNet-TS ($N = 1$)	35.71 ± 0.12	0.918 ± 0.001	0.094 ± 0.002
Intermediate	UNet-TS ($N = 4, M$)	35.90 ± 0.12	0.920 ± 0.001	0.091 ± 0.002
Intermediate	UNet-T ($N = 1$)	36.38 ± 0.12	0.927 ± 0.001	0.081 ± 0.002
Intermediate	UNet-T ($N = 4, M$)	36.39 ± 0.12	0.926 ± 0.001	0.081 ± 0.002
Center	UNet-TX ($N = 1$)	36.82 ± 0.09	0.946 ± 0.001	0.051 ± 0.001
Center	UNet-TX ($N = 4, M$)	37.04 ± 0.07	0.947 ± 0.001	0.050 ± 0.001
Center	UNet-TS ($N = 1$)	38.06 ± 0.09	0.955 ± 0.001	0.037 ± 0.001
Center	UNet-TS ($N = 4, M$)	38.16 ± 0.08	0.956 ± 0.001	0.035 ± 0.001
Center	UNet-T ($N = 1$)	39.11 ± 0.09	0.962 ± 0.001	0.025 ± 0.001
Center	UNet-T ($N = 4, M$)	39.04 ± 0.08	0.962 ± 0.000	0.025 ± 0.001

Table 11: Quantitative results for the Canon 24mm f/1.4L USM lens opened at f/1.4 [5].

on a UNet-T to improve the pooling function p between max pooling (M), lambda layer (L) and self-attention (A), and two stack sizes N in $\{4, 16\}$. More refined strategies to predict a better global feature g leads to results comparable to MIMOUNet [10] whereas the initial UNet-T hardly produces satisfactory results.

D.3 Optical aberration

We show qualitative examples synthesized with the 16mm and 24mm lenses from [5]. We show results of remove of the aberrations in the corner in Figures 12, 13 and 14. Even small details and textures that seem lost because of the aberrations may be salvaged with the collaborative scheme.

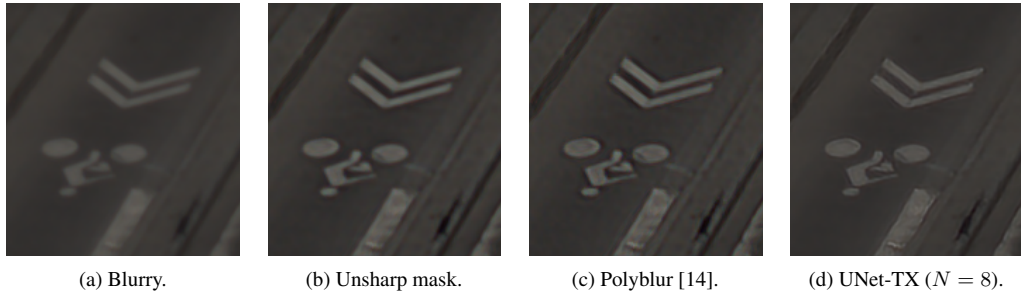


Figure 8: Sharpening example taken from the “Friant” image obtained with the online demo of [25].

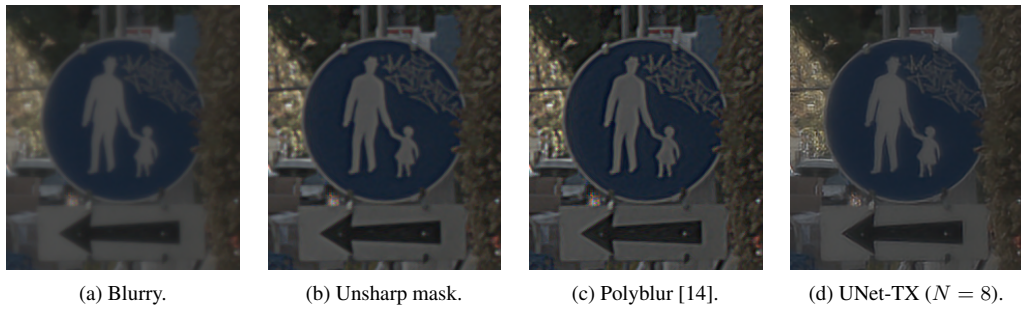


Figure 9: Sharpening example taken from the “Zurich” image obtained with the online demo of [25].

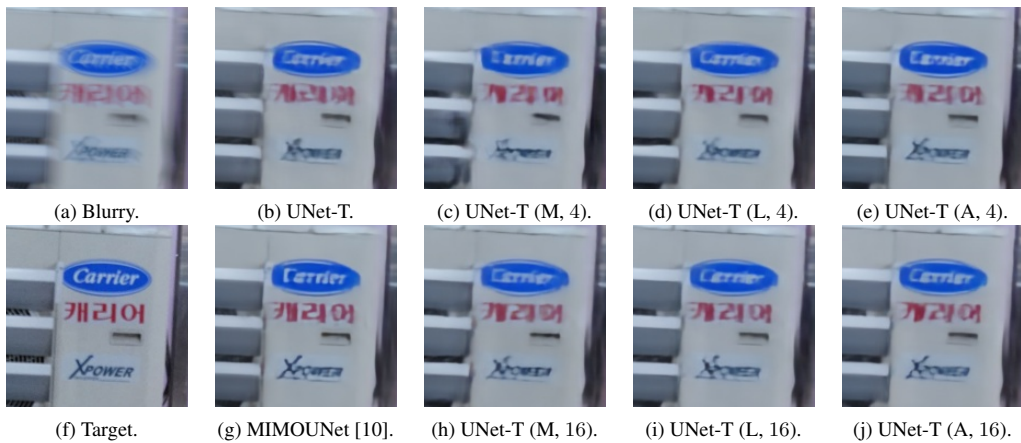


Figure 10: Camera shake removal from the Realblur-J test set [38]. Please zoom on a computer screen.

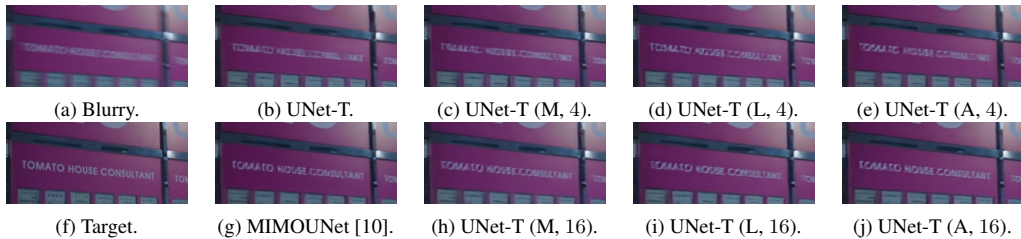


Figure 11: Camera shake removal from the Realblur-J test set [38]. Please zoom on a computer screen.

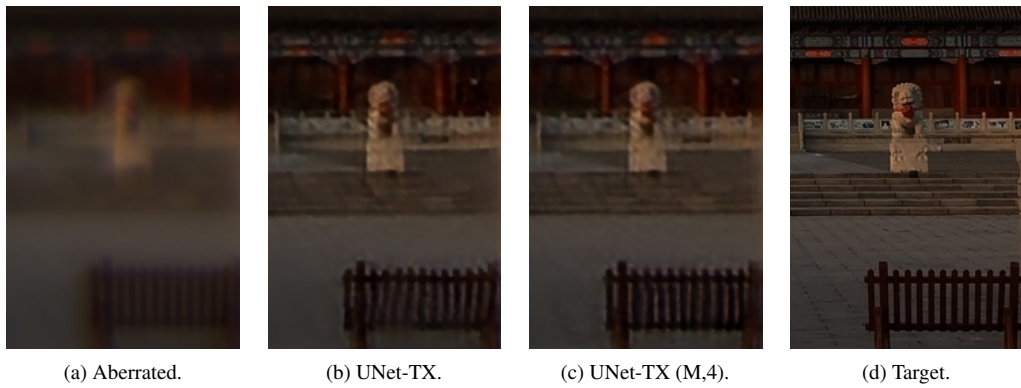


Figure 12: Aberration removal example for the Canon 16-35mm f2.8L USM EI lens from [5].

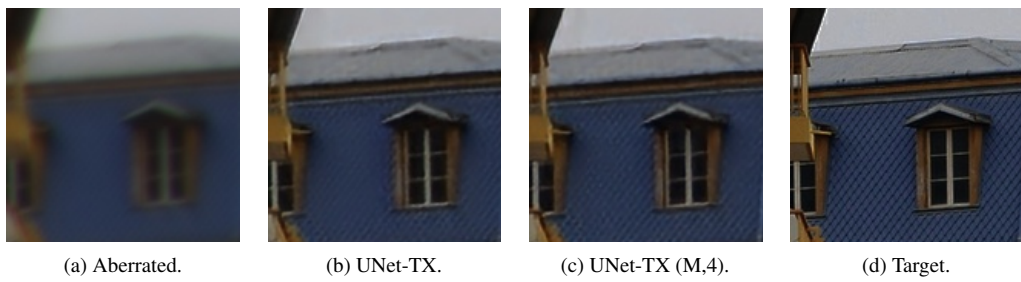


Figure 13: Aberration removal example for the Canon 24mm f1.4L USM lens from [5].

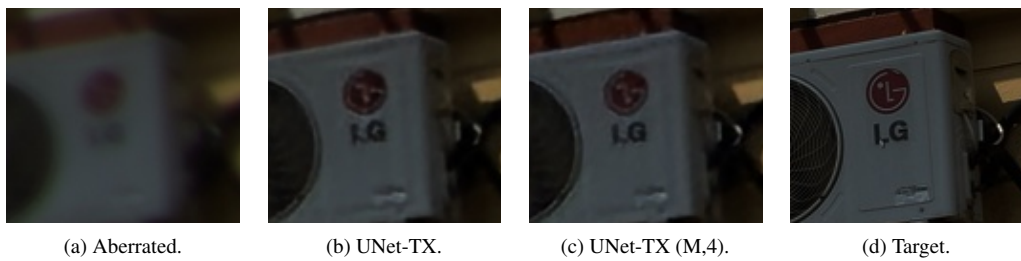


Figure 14: Aberration removal example for the Canon 24mm f1.4L USM lens from [5].